Materials Advances

ROYAL SOCIETY OF CHEMISTRY

PAPER

View Article Online
View Journal | View Issue

Check for updates

Cite this: *Mater. Adv.*, 2022, 3, 7595

Customizing the spatial distribution and release of silver for the antibacterial action *via* biomineralized self-assembling silver-loaded hydroxyapatite†

Yunping Qiao,[a] Guangqing Mai,[a] Yujing Li,[a] Rengui Guan,[a] Yanyang Han,[a] Wei Cui,[a] Xinglong Wang,[a] Shiliang Liu,[b] Shanshan Liu *[a] and Tao He*[a]

Received 13th March 2022,
Accepted 26th July 2022

DOI: 10.1039/d2ma00291d

rsc.li/materials-advances

The fabrication of a rationally designed silver-loaded hydroxyapatite (Ag–HA) material to balance antibacterial activity, biological safety and chemical stability is a significant challenge. The key to solving this problem lies in controlling the release of Ag^+ ions. This ambition has been skillfully fulfilled by a layer-by-layer self-assembly approach *via Staphylococcus aureus* (*S. aureus*)-templated mineralization. The abundant functional groups, namely teichoic acid and carboxyl groups, on *S. aureus* could induce the nucleation and growth of Ag–HA because of the strong chelating effect on the Ca^{2+} and Ag^+ ions. The spatial distribution of silver in Ag–HA microspheres has been designed by modifying the sedimentary order of the Ag^+ and Ca^{2+} ions. The as-prepared samples were characterized by XRD, SEM, EDS, TEM, XPS, FT-IR and Zate potential methods. The release of Ag^+ ions was measured by atomic absorption spectrometry. The results indicate that the derived Ag–HA hybrid antibacterial materials do not only inherit the uniform size of the *S. aureus* template well but also exhibit customized spatial distribution and release of Ag^+ ions.

Open Access Article. Published on 05 August 2022. Downloaded on 5/4/2026 2:56:22 AM.
This article is licensed under a Creative Commons Attribution-NonCommercial 3.0 Unported Licence.

1. Introduction

The invasion of microorganisms and viruses not only threatens human lives and health but also affects social and economic development. Developing new antibacterial materials is of great significance for preventing the spread of pathogenic microorganisms.[1,2] Because of safety and durability, inorganic antibacterial materials (silver, copper, zinc oxide, titanium dioxide, copper oxide) have greatly attracted the attention of chemical and biological researchers.[3] Especially, Ag-based antibacterial materials (Ag^+, Ag nanoparticles) are widely used in food packaging, plastic products, paints, coatings, textiles, medical equipment and medical dressings[4–7] due to their high and broad-spectrum antibacterial activity, as well as low toxicity to mammalian cells.[8]

However, owing to the photochemical activity, high solubility and oxidability of silver ions (Ag^+ ions), the application of silver-based antibacterial materials is limited. Accurately controlling the release rate of Ag^+ ions is crucial to mitigate these drawbacks. At present, although loading Ag^+ ions on an inert matrix (zirconium phosphate, silica, or zeolite) is the usual approach to inhibit chemical reactions with the environment or media,[9–12] employing structural design to control the release of silver from materials is still in the infancy stage.[13] For example, Ag^+ ions were absorbed by the mesoporous molecular sieve SBA-15[14] and also imported to zirconium phosphate or bentonite materials by the ion-exchange method;[10,11] yet, in these cases, the Ag^+ ions are released quickly due to the porous structure and weak interactions,[15] failing to realize sustained antibacterial action. Moreover, the burst release of silver increased the concentration of Ag^+ ions significantly in a short time, bringing about biological toxicity. In order to decrease the release rate of Ag^+ ions, hydrothermal and high-temperature sintering methods were applied to insert Ag^+ ions into the zirconium phosphate lattice.[16,17] However, the high-temperature conditions increased the size of the matrix particles, resulting in an excessively low release rate of Ag^+ ions. The antibacterial activity decreased eventually.

Hence, we believe that designing and synthesizing silver-based antibacterial materials with controllable silver ion release rates is the key to balancing antibacterial properties (antibacterial activity and durable antibacterial), biological safety and chemical stability. Generally, the release rate of Ag^+ ions mainly depends on the following factors: Firstly, the chemical state of silver (elemental Ag, soluble Ag^+ ions and insoluble silver salt) affects the release rate of silver ions.[5]

[a] College of Chemistry and Chemical Engineering, Yantai University, Yantai 264005, China. E-mail: liushanshan@ytu.edu.cn, ytuht@ytu.edu.cn
[b] Weifang Branch Company, Shandong HI-speed Transportation Construction Group Co., Ltd, Qingzhou, 262500, China

† Electronic supplementary information (ESI) available. See DOI: https://doi.org/10.1039/d2ma00291d

© 2022 The Author(s). Published by the Royal Society of Chemistry

Open Access Article. Published on 05 August 2022. Downloaded on 5/4/2026 2:56:22 AM.
This article is licensed under a Creative Commons Attribution-NonCommercial 3.0 Unported Licence.

Secondly, the diversity of Ag spatial distribution in the matrix particles leads to differences in diffusion resistance. Additionally, large particle and small specific surface also bring about high diffusion resistance for Ag^+ ions.[18–20] To sum up, precisely regulating the composition, structure and morphology of Ag-based antibacterial materials at the molecular level and nanoscale is the fundamental strategy for achieving the controlled release of Ag^+ ions.

Due to its biocompatibility, biodegradability and thermal stability, hydroxyapatite (HA) is not only an excellent candidate for bone repair and drug delivery but also a suitable inert matrix for Ag^+ ions.[21–23] For example, as a tooth or bone repairing material, HA doped with Ag^+ ions can inhibit the formation of bacterial membranes and mitigate the risk of wound infection.[24] The common methods for preparing Ag-loaded HA (Ag–HA) antibacterial materials are ion doping[25] and surface deposition.[26,27] However, neither of these methods has achieved controllable Ag^+ ion distribution and HA particle morphology. This work provides a self-assembling biomineralization approach to customize Ag–HA nanoparticles with different spatial distributions of Ag, based on which the controllable release of Ag^+ ions can be realized. The particle size of the synthesized Ag–HA antibacterial nanoparticles was uniform and controllable owing to the microbial template. Microbial cells (bacteria, fungi, and microalgae) display uniform morphology and size, which are dominated by genes and do not change under different culture conditions. On the other hand, the surface of microbial cells is usually negatively charged,[28,29] and the functional groups (carboxyl, amino, sulfhydryl, and hydroxyl) on the surface can form strong chemical bonds with metal ions, thus providing sites for the heterogeneous nucleation and growth of inorganic compounds. In addition, being a mature microbial technology, microbial cultures ensure the large-scale preparation of microbial cells. Therefore, microorganisms are the ideal templates for preparing inorganic particles with uniform size and morphology. So far, yeast and *Escherichia coli* (*E. coli*) cells have been employed as templates to prepare hollow spheres, zinc oxide tubes, zirconia and titanium dioxide porous structure.[30–34] Nevertheless, the preparation of an Ag–HA antibacterial material with the controllable spatial distribution of Ag to regulate the release rate of Ag^+ ions has not been reported. For the construction of Ag–HA antibacterial materials with the controllable spatial distribution of Ag, *Staphylococcus aureus* (*S. aureus*), the surface of which contains abundant teichoic acid and carboxyl groups, was used as the template. These functional groups have a strong chelating effect on Ag^+ and Ca^{2+} ions and can induce nucleation. The Ag^+ and Ca^{2+} ions were alternately deposited on the *S. aureus* templates layer by layer. The spatial distribution of Ag in a single Ag–HA microsphere was customized by modifying the order of Ag^+ and Ca^{2+} ion addition. Consequently, Ag–HA antibacterial materials with different release rates of Ag^+ ions were obtained. This work provides a new perspective and strategy for the development of advanced HA-based biomedical materials with antibacterial properties.

2. Experimental details

2.1 Preparation of silver-loaded hydroxyapatite antibacterial nanoparticles

The traditional microbial experiment technology was applied for the *S. aureus* culture.[35] The core-shell structured Ag–HA

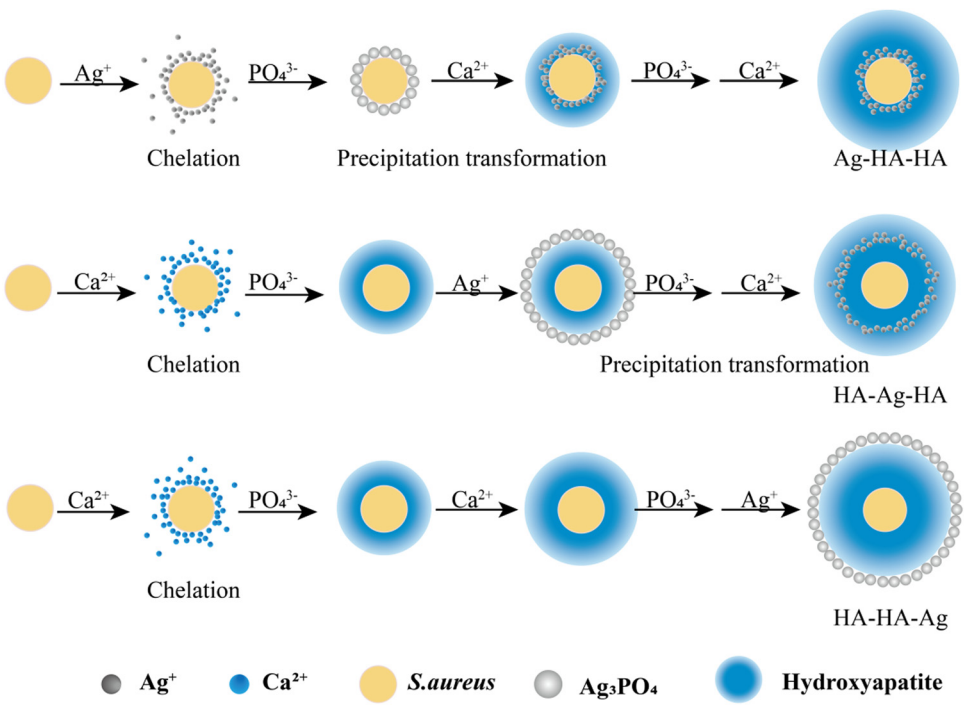

Fig. 1 The preparation of antibacterial Ag-loaded hydroxyapatite (HA) by the ionic layer-by-layer self-assembly method with *S. aureus* as the template.

© 2022 The Author(s). Published by the Royal Society of Chemistry

Open Access Article. Published on 05 August 2022. Downloaded on 5/4/2026 2:56:22 AM.
This article is licensed under a Creative Commons Attribution-NonCommercial 3.0 Unported Licence.

antibacterial nanoparticles (Ag–HA–HA, HA–Ag–HA, HA–HA–Ag) with different spatial distributions of Ag were prepared by ionic layer-by-layer self-assembly method at room temperature, as shown in Fig. 1, by employing *S. aureus* as the template.

The specific experimental procedures were as follows (Fig. 2):

Step 1: 20 mL *S. aureus* culture ($\sim 10^9$ CFU mL^{-1}) was mixed with 10 mL $AgNO_3$ (0.01 g mL^{-1}), 10 mL $Ca(NO_3)_2$ (0.225 M), and 10 mL $Ca(NO_3)_2$ (0.225 M) under mechanical stirring to obtain the S_1, S_1', and S_1'' suspensions, respectively.

Step 2: The S_1, S_1' and S_1'' suspensions were mixed with 80 mL Na_2HPO_4 solution (pH = 12), and the mixtures were stirred for 20 min to form the S_2, S_2', and S_2'' suspensions, respectively.

Step 3: 10 mL $Ca(NO_3)_2$ solution (0.225 M), 10 mL $AgNO_3$ solution (0.01 g mL^{-1}) and 10 mL $Ca(NO_3)_2$ solution (0.225 M) were separately added dropwise to the S_2, S_2', S_2'' suspensions under stirring to form the S_3, S_3', and S_3'' suspensions, respectively.

Step 4: 10 mL of a Na_2HPO_4 solution (0.14 M and pH = 12) was added dropwise to S_3, S_3', and S_3'' to prepare the S_4, S_4', and S_4'' suspensions, respectively.

Step 5: 10 mL $Ca(NO_3)_2$ solution (0.225 M),10 mL $Ca(NO_3)_2$ solution (0.225 M) and 10 mL $AgNO_3$ solution (0.01 g mL^{-1}) were added dropwise to solutions S_4, S_4', and S_4'' to obtain the S_5, S_5', and S_5'' suspensions, respectively.

Afterward, the S_5, S_5', and S_5'' solutions were centrifuged respectively, and a sodium chloride solution was added to the supernatant. No precipitation was observed, indicating that the Ag^+ ions were loaded on hydroxyapatite completely.

Step 6: The S_5, S_5', and S_5'' solutions were centrifuged at 4500 rpm for 3 min and washed three times with 30 mL absolute ethanol, respectively. Afterwards, the particles were dissolved in 30 mL polyethylene glycol-400 by the ultrasonic dispersion method. The dispersions were heated at 220 °C for 10 minutes followed by centrifugation for 3 minutes at 4000 rpm. The precipitates were washed three times with absolute ethanol. Finally, the precipitates were dried at 60 °C to obtain the three silver-loaded hydroxyapatite powder samples, namely Ag–HA–HA, HA–Ag–HA, and HA–HA–Ag.

2.2 Sample characterization

The as-prepared samples were characterized by X-ray diffraction (XRD, Rigaku Smart Lab III), scanning electron microscopy (SEM, JEOL JSM-7900F), energy-dispersive spectroscopy Mapping (EDS, OXFORD, ULTIM EXTREME), transmission electron microscopy (TEM, JEOL JEM-2100F), X-ray photoelectron spectroscopy (XPS, Thermo ESCALAB 250xi), Fourier transform infrared spectroscopy (FT-IR, SHIMADZU IRAffinity-1S) and Zeta potential analysis (Zetasizer Nano force potentiometer, Malvern Nano-ZS90).

2.3 Antibacterial activity measurements

The release of Ag was studied by atomic absorption spectrometry (AAS, TAS-990super). The measurement details are described in the ESI† (ESI,† Release of Ag). The minimum inhibitory concentration (MIC),[36] minimum bactericidal concentration (MBC), the kinetics of inactivation and microbial growth inhibition (ESI,† inhibition zone experiment)[37] were evaluated to characterize the antibacterial performance.

3. Results and discussion

3.1 Zeta potential

In order to monitor the deposition of the ions on the template surfaces, the Zeta potential was measured at each step (Fig. 3). Taking the HA–Ag–HA particles as an example, the Zeta potentials of the particle surface in the *S. aureus* solution, and the S_1', S_2', S_3', S_4', and S_5' solutions were measured, respectively. As shown in Fig. 3, all the particles were negatively charged, and interparticular repulsion could effectively inhibit particle aggregation. When the HA–Ag particles were prepared without the *S. aureus* templates according to the procedure described in the experimental section (ESI,† Ag–HA prepared by the co-precipitation method), the HA–Ag nanocrystals agglomerated greatly (Fig. S1, ESI†), indicating

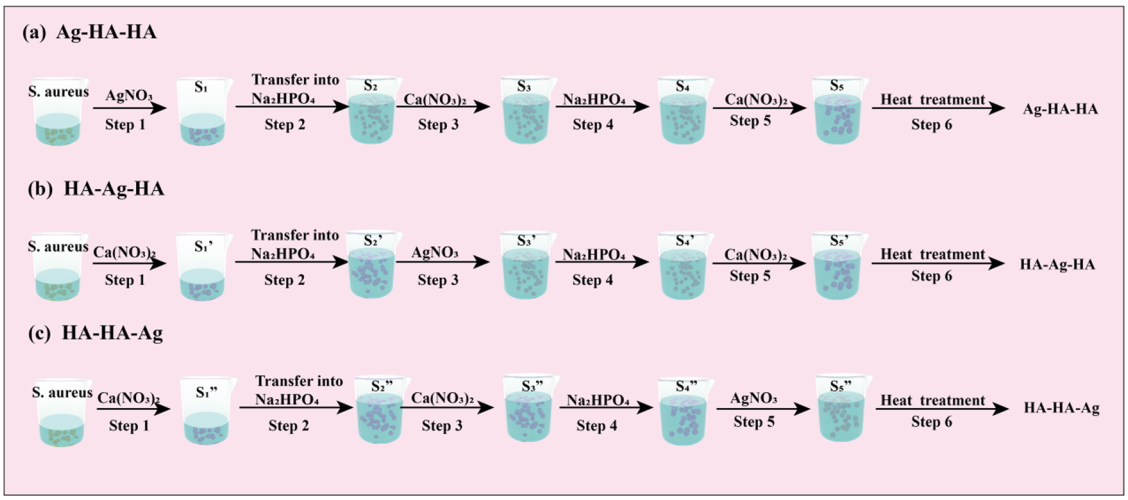

Fig. 2 Schematic of the step-by-step procedure of preparing the Ag–HA antibacterial particles: (a) Ag–HA–HA (b) HA–Ag–HA and (c) HA–HA–Ag.

Open Access Article. Published on 05 August 2022. Downloaded on 5/4/2026 2:56:22 AM.
This article is licensed under a Creative Commons Attribution-NonCommercial 3.0 Unported Licence.

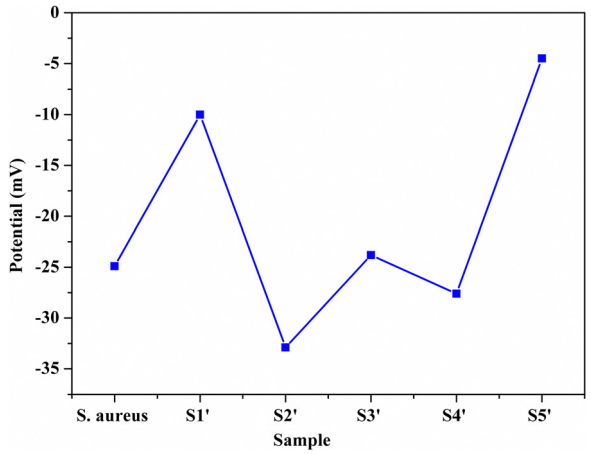

Fig. 3 . Zeta potential during the preparation of the HA–Ag–HA sample.

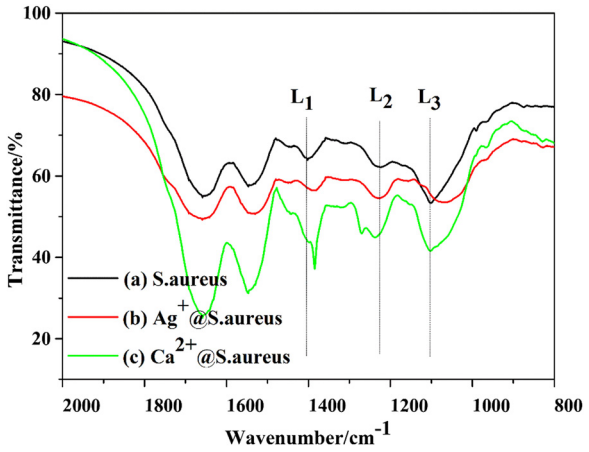

Fig. 5 The FT-IR spectra of (a) *S. aureus*, (b) Ag^{+}@*S. aureus* and Ca^{2+}@*S. aureus*.

that the participation of the *S. aureus* templates effectively inhibited aggregation.

Initially, the surface of the *S. aureus* template is negatively charged due to the teichoic acid on the surface. After adding $Ca(NO_3)_2$ (S_1' solution), the Ca^{2+} cations are chelated by the teichoic acids on *S. aureus* (Ca^{2+}@*S. aureus*), and the potential increases. With the addition of Na_2HPO_4, in the S_2' solution, the OH^- and PO_4^{3-} ions react with the Ca^{2+} ions on the *S. aureus* to form HA@*S. aureus*. The excessive PO_4^{3-} ions decrease the surface potential of the particles obviously. Afterwards, with the addition of $AgNO_3$, in the S_3' solution, the Ag^{+} ions precipitate on the particle surface (Ag_3PO_4/HA@*S. aureus*) owing to the PO_4^{3-} ions. The excessive Ag^{+} ions slightly increase the surface potential. After adding Na_2HPO_4 again, in the S_4' solution, the PO_4^{3-} ions react with the Ag^{+} ions on the particle decreasing the potential again. Finally, when $Ca(NO_3)_2$ is added, the S_5' solution demonstrates substantially increased potential due to the deposition of Ca^{2+} ions.

Although biotemplate routes have been extensively applied for the preparation of inorganic nanostructures,[31,33,38,39] the controllable space distribution of certain metal ions (Ag^{+}) in inorganic carrier particles has not been realized through the simple biotemplate method. Intentionally utilizing the natural functional groups on the templates as nucleation sites to induce inorganic nanostructures is an effective approach to controlling the distribution of ions. In this work, the Zeta potential results showed that the Ca^{2+}, PO_4^{3-} and Ag^{+} ions were deposited on the *S. aureus* templates alternately. The formation of the Ag–HA particles was carried out by the layer-by-layer mineralization of ions on the *S. aureus* templates (Fig. 4). The strong chelation of *S. aureus* to the metal ions (Ca^{2+} or Ag^{+} ions) provides the nucleation sites for HA–Ag particles due to the teichoic acid and carboxyl groups, followed by the layer-by-layer encapsulation of the *S. aureus* templates by the ions.

3.2 FT-IR

FT-IR spectroscopy is a reliable technique to analyze the chemical bonds or functional groups involved in proteins, fatty acids, carbohydrates, nucleic acids, and lipopolysaccharides of bacteria. In order to further confirm the biotemplate role of *S. aureus*, the FT-IR spectra of the precipitates Ag^{+}@*S. aureus* from the S_1 suspension, Ca^{2+}@*S. aureus* from the S_1' suspension and *S. aureus* were collected after freeze drying (ESI,† FT-IR), respectively (Fig. 5). Herein, we focused on the three bands located at 1398.9 (L_1), 1223.7 (L_2) and 1134–980 (L_3) cm^{-1}, which correspond to different groups,[40] as demonstrated in Table 1. The L_1 band was derived from the COO^- groups. Compared with the spectrum of *S. aureus*, the L_1 bands of both Ag^{+}@*S. aureus* and Ca^{2+}@*S. aureus* had shifted to lower wavenumbers, indicating that the Ag^{+} or Ca^{2+} ions interacted with the COO^- groups. Besides, the L_2 band of Ca^{2+}@*S. aureus* was split into two bands due to the chemical interactions between Ca^{2+} and phospholipids. The L_3 band of Ag^{+}@*S. aureus* had shifted to a lower wavenumber because of the chemical interactions formed between the Ag^{+} ions and phospholipids.[40] Therefore, the FT-IR results confirm that the Ag^{+} and Ca^{2+} ions were anchored on the *S. aureus* templates *via* different absorption mechanisms. Both Ag^{+} and Ca^{2+} ions apparently interact with the functional groups on *S. aureus*, which effectively provides nucleation sites for Ag–HA particles. Thus, Ag–HA

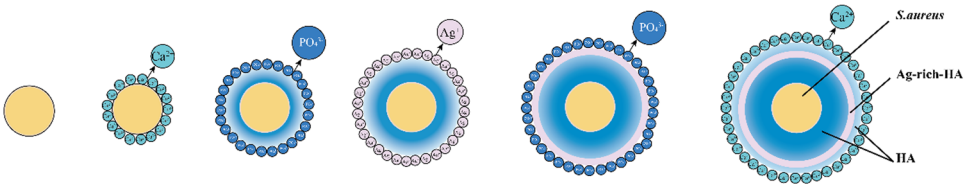

Fig. 4 Illustration of the layer-by-layer assembly of ions on the *S. aureus* template.

© 2022 The Author(s). Published by the Royal Society of Chemistry

Open Access Article. Published on 05 August 2022. Downloaded on 5/4/2026 2:56:22 AM.
This article is licensed under a Creative Commons Attribution-NonCommercial 3.0 Unported Licence.

Table 1 Assignments of the absorption bands

Band	Wavenumber (cm^{-1})	Assignment
L_1	1398.9	COO^- groups in amino acids, fatty acids
L_2	1223.7	P═O of phosphodiesters in phospholipids
L_3	1134–980	P═O in DNA, RNA and phospholipids

nucleates and grows on *S. aureus* templates and encapsulates them finally.

3.3 XRD

The phase composition of the Ag–HA particles Ag–HA–HA, HA–Ag–HA and HA–HA–Ag was determined by the XRD method. Further, the transformation of phase composition in each step was also monitored (ESI,† XRD step-by-step). The XRD patterns obtained at each step of the Ag–HA–HA, HA–Ag–HA and HA–HA–Ag sample synthesis are presented in Fig. 6.

The XRD patterns of the Ag–HA–HA sample are shown in Fig. 6a. Ag_3PO_4 was formed after loading the Ag^+ cations and PO_4^{3-} ions (Step2-S_2) on the *S. aureus* templates, but with the addition of the Ca^{2+} cations and PO_4^{3-} ions (Step3-S_3, Step4-S_4), the peaks of the (210) and (211) planes of Ag_3PO_4 gradually decreased, and the characteristic peaks of planes (002), (211), (112) of HA gradually appeared. Finally, the characteristic peaks of Ag_3PO_4 were hardly observed. The XRD patterns in Step1-S_1' and Step2-S_2' of the HA–Ag–HA sample in Fig. 6b indicate that amorphous HA was formed with the addition of Ca^{2+} and PO_4^{3-}. The characteristic peaks of the (210) and (211) planes of Ag_3PO_4 in the Step4-S_4' spectrum suggest that Ag_3PO_4 was formed with the addition of the Ag^+ ions (Step3-S_3') and PO_4^{3-} ions (Step4-S_4'). However, with the addition of the Ca^{2+} ions (Step5-S_5'), the characteristic peak of Ag_3PO_4 also disappeared.

The reason for the disappearance of the Ag_3PO_4 phase in the Ag–HA–HA and HA–Ag–HA samples is that the product solubility constant (K_{sp}(HA) = (6.3 ± 2.1) × 10^{-59}, 25 °C) of HA is much lower than that (K_{sp}(Ag_3PO_4) = 8.89 × 10^{-17}, 25 °C) of Ag_3PO_4, and precipitation transformation occurs with the addition of Ca^{2+} (Fig. 7). After an excess of Ca^{2+} ions was added, most Ag_3PO_4 was converted to HA and Ag^+ ions. Moreover, in the whole experiment, the PO_4^{3-} ions were in excess relative to the Ag^+ ions, and there were no dissociative Ag^+ ions in the final supernatant. Hence, it can be concluded that all the Ag^+ ions generated from the precipitation transformation were *in-situ* loaded in the HA shell. The Ag^+ ions were distributed in the inner HA shell of the Ag–HA–HA sample and the middle HA shell of the HA–Ag–HA sample. Generally, Ag^+ ions are easily reduced to Ag NPs because of strong oxidability. Many efforts have been devoted to the development of Ag NP-encapsulated porous materials, such as mesoporous silica and zeolite.[13–16,41] Liu *et al.*[42] prepared Ag-MMT with high dispersivity, narrow size distribution and good thermal stability by chemical reduction and the supercritical ethanol drying method. In this experiment, the XRD spectra of Ag–HA–HA and HA–Ag–HA showed no diffraction peaks for any silver phase, indicating that silver mainly existed in the form of Ag^+ ions embedded in the HA framework, and the reduction is avoided effectively.

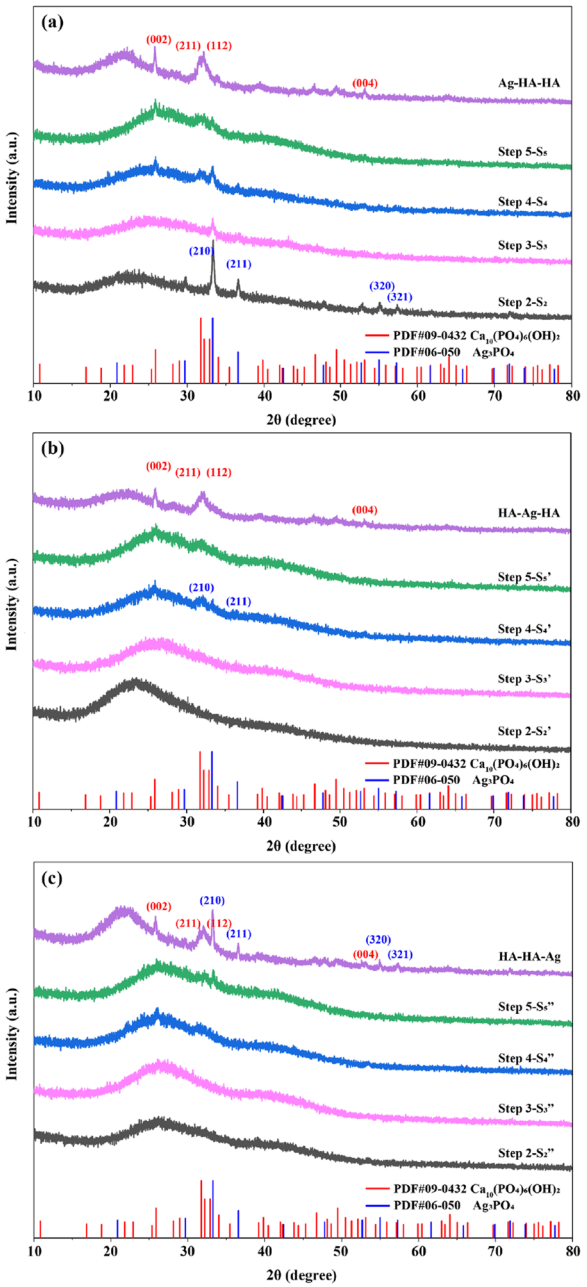

Fig. 6 Determination of the phase evolution during Ag–HA particle preparation using XRD: (a) Ag–HA–HA, (b) HA–Ag–HA, and (c) HA–HA–Ag.

As demonstrated by the XRD patterns of the HA–HA–Ag sample in Fig. 6c, only amorphous HA was present before Ag^+ was loaded (Step5-S_5''), and Ag_3PO_4 was gradually formed with the addition of Ag^+ ions. The XRD pattern of the final HA–HA–Ag sample showed strong Ag_3PO_4 peaks, indicating that silver in the particles existed mainly in the Ag_3PO_4 phase, which is different from Ag–HA–HA and HA–Ag–HA samples. During the preparation of HA–HA–Ag, Ag^+ ions are added at the last and reacted with PO_4^{3-} ions on the surface of the particles. There was no further precipitation transformation because trace or no Ca^{2+} ions existed in the solution.

Owing to the heating treatment in Step 4, the final Ag–HA–HA, HA–Ag–HA and HA–HA–Ag samples presented better

Open Access Article. Published on 05 August 2022. Downloaded on 5/4/2026 2:56:22 AM.
This article is licensed under a Creative Commons Attribution-NonCommercial 3.0 Unported Licence.

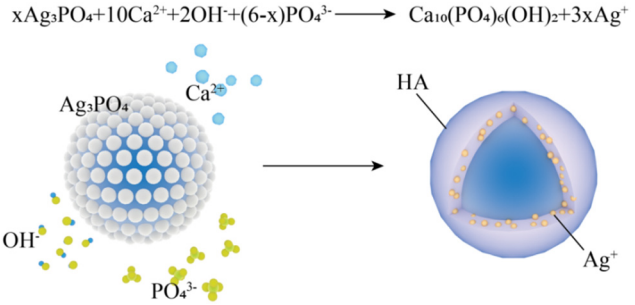

Fig. 7 Illustration of precipitation transformation from Ag_3PO_4 to HA.

crystallization. The XRD patterns of all the final samples showed the (002), (211), (122) and (004) diffraction peaks of HA, confirming that the final material was HA. However, the intensity of peaks was very weak and wide. The (211) and (112) peaks were overlapping, suggesting that the crystallinity of HA was low or it mainly existed in an amorphous state.

The *S. aureus* templates play a very important role in realizing the controllable growth of nanostructures. Carmen Steluta Ciobanu *et al.* synthesized antibacterial Ag-doped nano-hydroxyapatite nanocrystallites at 100 °C by co-precipitation,[43] in which HA was evidently crystalline. Herein, the metal ions (Ca^{2+}, Ag^{+}) can be anchored solidly on the *S. aureus* templates due to strong chelation. As a result, the ordered arrangement of the crystal structure may be impeded, resulting in low crystallinity or even an amorphous structure. In order to verify this point, the co-precipitation method without the *S. aureus* templates was used to prepare the Ag–HA materials (ESI,† Ag–HA prepared by co-precipitation method). It was found that all the Ag–HA samples prepared by the co-precipitation method without templates showed apparent crystalline phases, including the $AgPO_4$ and HA phases (Fig. S2, ESI†). Therefore, the biomineralization route using the *S. aureus* templates can prevent the crystallization of the HA and Ag phases effectively.

3.4 XPS

In order to further confirm the chemical state and distribution of Ag, the XPS spectra of the Ag–HA–HA, HA–Ag–HA, and HA–HA–Ag particles were collected. All three particles contained Ca, P, Ag, and O elements, as shown in Fig. 8a–c, respectively. Their corresponding fine Ag3d orbital spectra are shown in Fig. 8d–f. The two characteristic peaks of the spin orbits $Ag3d_{3/2}$ and $Ag3d_{5/2}$ were located at 373.5 and 367.5 eV, respectively. The difference between the two characteristic peaks was 6.0 eV, proving that silver existed in the form of Ag(I).[43–45] On the other hand, for solid samples, the XPS method can reflect the mole percentage of each element on the ultra-surface in the depth range of less than 10 nm. The results show that the atomic ratio of Ca/Ag, P/Ag and O/Ag on the surface (Table 2) increased in the sequence of Ag–HA–HA → HA–Ag–HA → HA–HA–Ag because Ag was mainly distributed in the inner layer of Ag–HA–HA, the middle layer of HA–Ag–HA, and the surface layer for HA–HA–Ag. In brief, the spatial distribution of Ag was different in the Ag–HA–HA, HA–Ag–HA, and HA–HA–Ag particles.

3.5 SEM and EDS

The SEM images are shown in Fig. 9. All the particles were spherical with a uniform diameter of about 500 nm. Each sphere surface was rough and dense and was stacked in the

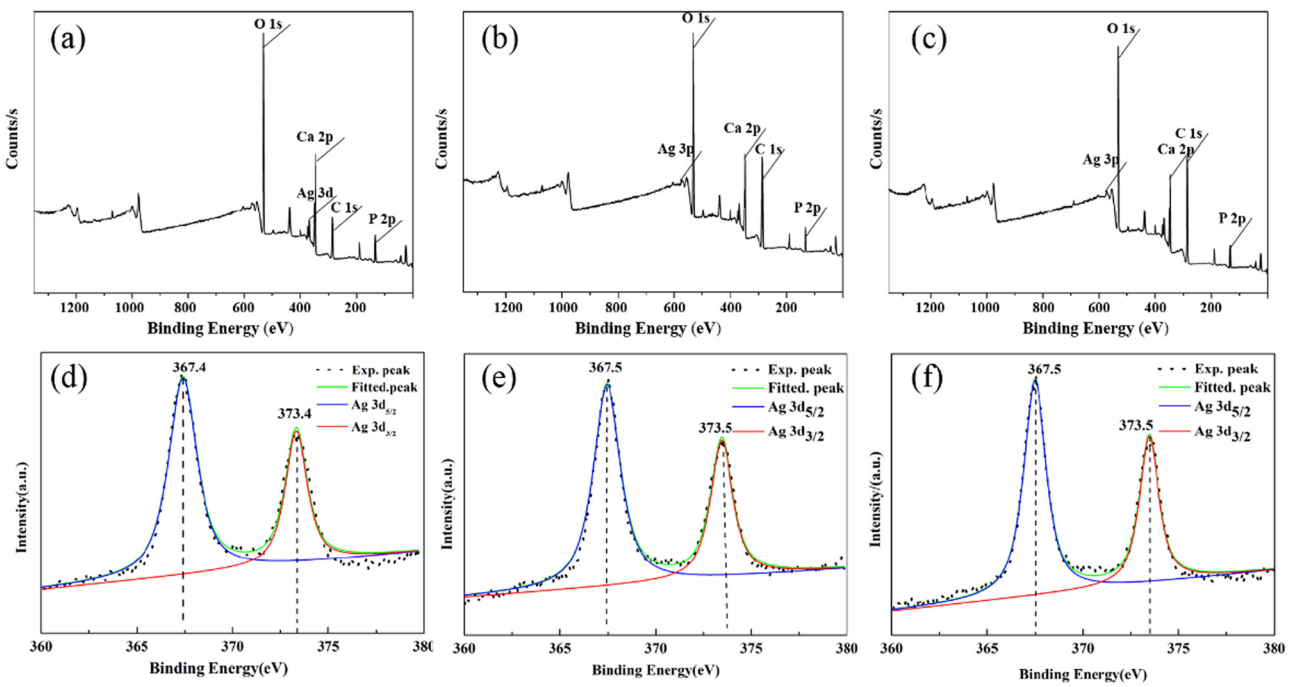

Fig. 8 X-Ray photoelectron spectra of the samples: General spectrum of (a) Ag–HA–HA, (b) HA–Ag–HA, and (c) HA–HA–Ag. Deconvolution of the Ag3d XPS peaks of (d) Ag–HA–HA(d), (e) HA–Ag–HA and (f) HA–HA–Ag.

© 2022 The Author(s). Published by the Royal Society of Chemistry

Open Access Article. Published on 05 August 2022. Downloaded on 5/4/2026 2:56:22 AM.
This article is licensed under a Creative Commons Attribution-NonCommercial 3.0 Unported Licence.

Table 2 Atomic ratios of the elements on the surface of the samples

Sample	Ca/Ag	P/Ag	O/Ag
Ag–HA–HA	13.3	11.02	54.25
HA–Ag–HA	10.2	8.88	52.16
HA–HA–Ag	8.5	7.54	49.41

form of layered crystals because of the growth habits of HA. Fig. 10 shows the element distribution in the samples. Nitrogen (N) distribution shows the information about the *S. aureus* templates. The distributions of N, Ca, P and Ag prove that the synthesis of Ag–HA was based on the *S. aureus* cell templates. However, the distribution of Ag in the three samples was different. The Ag elemental distribution was relatively homogeneous on the Ag–HA–HA and HA–Ag–HA particles. The HA–HA–Ag particles obviously showed local Ag enrichment probably due to the Ag_3PO_4 particles, according to the XRD results.

Currently, Ag-based antibacterial materials are obtained by ion-exchange, co-precipitation, absorption and sintering methods.[46–52] However, according to the structure and morphology of the final products prepared by these routes, it is still very difficult to accurately control the particle size, dispersion and morphology of HA, as well as the spatial distribution of Ag in the HA particles. Herein, the size and morphology of the HA particles are precisely customized with uniform dispersion using the layer-by-layer biomineralization strategy. On the other hand, altering the order of Ca^{2+} and Ag^{+} ion addition not only can control the distribution of Ag but also can adjust the phase of silver.

3.6 TEM

The TEM image of the HA–Ag–HA particle in Fig. 11b shows a hollow structure, unlike those of Ag–HA–HA and HA–HA–Ag shown in Fig. 11a and c, respectively. The HA particles in all the samples were amorphous, which presents low contrast in TEM images. Hence, the difference in mass thickness contrast is not obvious for hollow structures. For the Ag–HA–HA particles, the high image contrast close to *S. aureus* in Fig. 11a suggests that Ag existed in the inner layer since the mass thickness contrast of Ag is much greater than those of calcium and phosphorus.

Although some Ag_3PO_4 nanoparticles appeared in the TEM images of the Ag–HA–HA (Fig. 11a) and HA–Ag–HA(Fig. 11b) particles, there was no Ag_3PO_4 phase according to XRD results. This is because the Ag element mainly exists in the form of Ag^{+} ions in the HA framework and only in trace amounts in the Ag_3PO_4 phase.

3.7 Silver ion release

The controlled release of Ag is critical for optimum antibacterial performance without cytotoxicity. In general, hydrothermal and high-temperature sintering methods are usually employed to synthesize Ag-loaded zirconium phosphate materials. Magana *et al.*[53] synthesized nano-silver-loaded montmorillonite by ion exchange and calcination at 400 or 550 °C. However, the silver particles loaded in the interlayer congregated at high temperatures, leading to a decrease in antibacterial activity. On the other hand, Ag resides mostly on the outer surface of the material prepared by the ion-exchange method and is quickly depleted without exerting a long-term antibacterial effect.[54] Hong Wu *et al.* synthesized self-detoxifying hollow zinc silica nanospheres with tunable Ag-ion-release–recapture capability at 500 °C.[55] In this study, the Ag–HA antibacterial materials have been prepared by a simple process and under mild reaction conditions (room temperature). Ag^{+} ion release from all the samples was investigated by the AAS method. The results are shown in Fig. 12. HA–Ag–HA had the highest Ag^{+} release rate and quantity, both of which were the lowest for HA–HA–Ag. This can be attributed to the diffusion, dissolution and state of the Ag^{+} ions. Specifically, silver exists mainly in the form of Ag^{+} ions in the HA–Ag–HA particles, from which Ag^{+} ions diffuse into the aqueous solution easily. The release rate of Ag^{+} ions in HA–HA–Ag was the lowest because of the particle-specific effect of the large $AgPO_4$ nanoparticles. Therefore, Ag–HA materials with different Ag phases, particle sizes, and spatial distributions

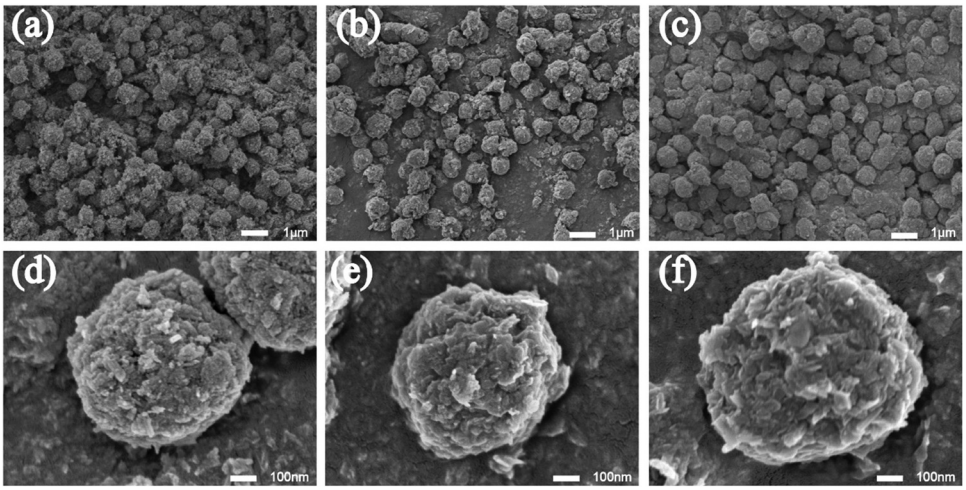

Fig. 9 The SEM images of the Ag–HA particles: (a, d) Ag–HA–HA, (b, e) HA–Ag–HA, (c and f) HA–HA–Ag.

Open Access Article. Published on 05 August 2022. Downloaded on 5/4/2026 2:56:22 AM.
This article is licensed under a Creative Commons Attribution-NonCommercial 3.0 Unported Licence.

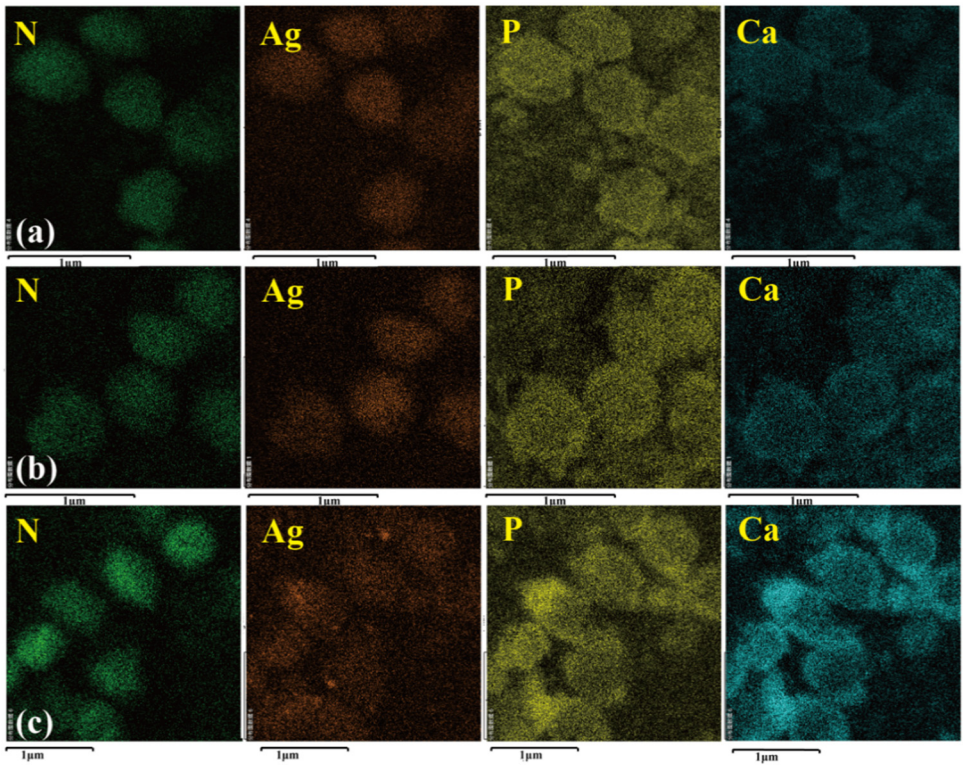

Fig. 10 The elemental distribution of the Ag–HA particles: (a) Ag–HA–HA, (b) HA–Ag–HA, and (c) HA–HA–Ag.

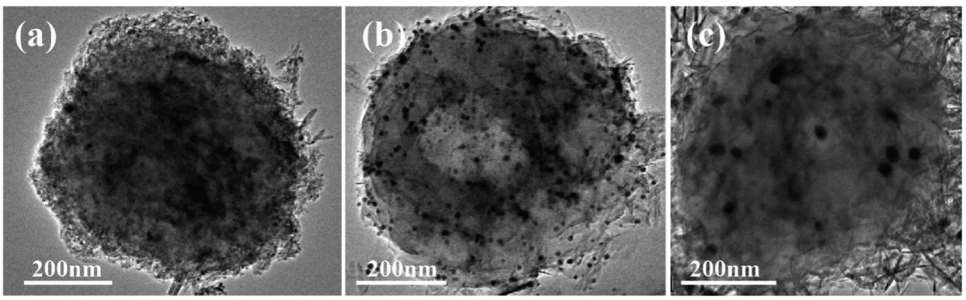

Fig. 11 The TEM images of the Ag–HA particles: (a) Ag–HA–HA, (b) HA–Ag–HA, and (c) HA–HA–Ag.

can lead to different release rates of Ag^+ ions, which can be tuned to meet different antibacterial requirements.

3.8 Antibacterial properties

3.8.1 MIC and MBC. *S. aureus* was used as the model bacterium for the antibacterial activity experiments. The MIC values of the Ag–HA–HA, HA–Ag–HA and HA–HA–Ag particles were 0.014 wt%, 0.007 wt% and 0.014 wt%, respectively. Moreover, the MBC of the Ag–HA–HA, HA–Ag–HA and HA–HA–Ag particles were 0.031 wt%, 0.031 wt% and 0.125 wt%, respectively (Fig. 13). HA–Ag–HA possessed the best antibacterial activity because of its excellent Ag^+ ion release performance.

3.8.2 Inactivation of *S. aureus*. Generally, the kinetics of inactivation is analyzed using the relationship based on the Chick–Watson model:[56,57]

$$\mathrm{Log}\,(N_t/N_0) = -kt$$

where N_0 is the initial *S. aureus* population, N_t is the population of *S. aureus* at time t, and k is the inactivation constant, which is the direct measure of antibacterial activity.

Fig. 14 shows the kinetics of the antibacterial activities of Ag–HA–HA, HA–Ag–HA and HA–HA–Ag, respectively. The bactericidal effect could be mainly attributed to Ag^+ ion dissolution. On account of the controlled release of Ag^+ ions, the kinetics of inactivation did not ideally accord with the Chick–Watson model.

When Ag–HA–HA was used to inactivate *S. aureus*, the population of bacteria slightly increased in 30 minutes and then decreased. The delayed bactericidal effect is mainly brought about by diffusion barriers. Since the Ag^+ ions are

© 2022 The Author(s). Published by the Royal Society of Chemistry

Open Access Article. Published on 05 August 2022. Downloaded on 5/4/2026 2:56:22 AM.
This article is licensed under a Creative Commons Attribution-NonCommercial 3.0 Unported Licence.

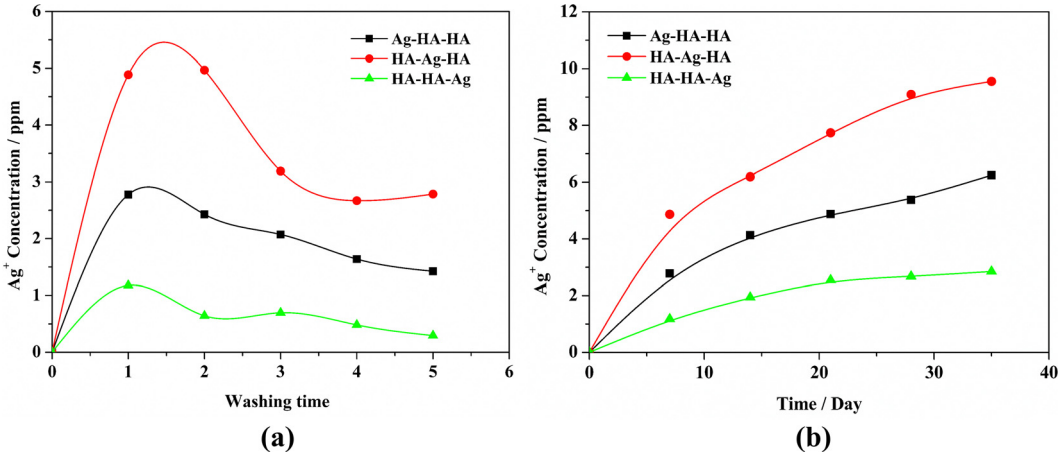

Fig. 12 . Ag^+ concentration with different soaking times(a) and soaking duration(b).

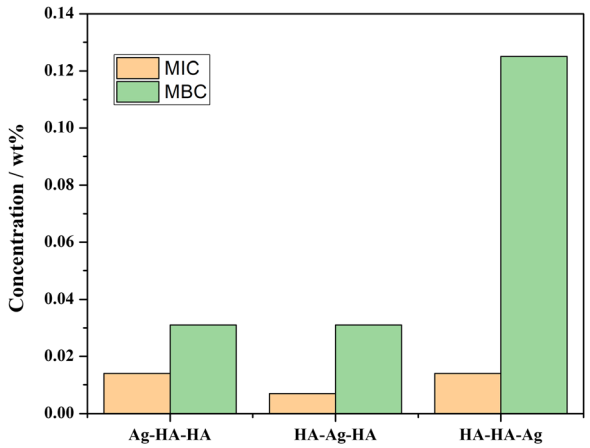

Fig. 13 MIC and MBC of Ag–HA–HA, HA–Ag–HA and HA–HA–Ag with *S. aureus* as the model bacterium.

distributed in the innermost layer of Ag–HA–HA particles, only after the Ag^+ ions spread from the inner layer and are exposed to the bacteria, the antibacterial activity can be achieved. The diffusion resistance was the highest in this case, resulting in the lowest inactivation rate.

The antibacterial activity of the HA–HA–Ag sample is ascribed to Ag_3PO_4 nanocrystallites located on the surface of particles. The exposure-dependent effect and low diffusion resistance lead to a higher microbial inactivation rate than that of Ag–HA–HA. This is the reason the antibacterial results disagree with the Ag^+ ions release rates of the Ag–HA–HA and HA–HA–Ag samples.

The HA–Ag–HA particles, in which the Ag^+ ions exist in the middle layer of the particles, possessed the highest inactivation rate. Synthetically, the lower diffusion resistance and easy dissolution of Ag^+ ions contribute to the highest inactivation rate.

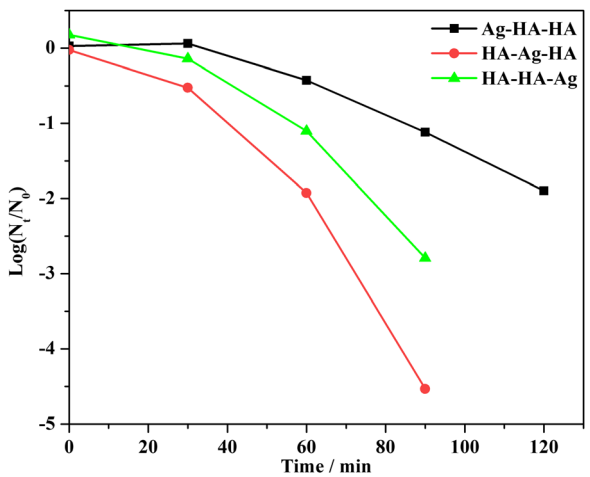

Fig. 14 *S. aureus* inactivation by Ag–HA–HA, HA–Ag–HA and HA–HA–Ag.

4. Conclusion

A self-assembling biomineralization approach at room temperature was applied to realize the controlled release of Ag^+ ions by customizing the spatial distribution of Ag in Ag-loaded HA (Ag–HA) hybrid materials. In the experiment, *S. aureus* templates with abundant teichoic acid functional groups on the surface could induce the nucleation and growth of HA because of the strong chelating ability with the metal ions. The Ag^+ and Ca^{2+} ions were alternately deposited on *S. aureus* templates layer by layer. The spatial distribution of Ag in a single Ag–HA microsphere was customized by modifying the deposition order of the Ag^+ and Ca^{2+} ions and precipitation transformation. This work has not only realized tunable Ag^+ release behavior in silver-based antibacterial materials but also the balance between antibacterial action and biological safety. A new perspective and strategy for the development of advanced HA biomedical materials with antibacterial properties are provided. Besides, durable silver-loaded HA materials with safe antibacterial properties can also be potential candidates for antibacterial textiles and antibacterial cosmetics. The development of biomedical materials involved in orthopedics, dentistry and medicine can be promoted using this strategy.

Open Access Article. Published on 05 August 2022. Downloaded on 5/4/2026 2:56:22 AM.
This article is licensed under a Creative Commons Attribution-NonCommercial 3.0 Unported Licence.

Conflicts of interest

There are no conflicts to declare.

Acknowledgements

This work is financially supported by the project ZR2020-MB069, ZR202103030521 supported by Natural Science Foundation of Shandong Province and National Natural Science Foundation of China (grant 51702034).

References

1 Z. A. Ratan, F. R. Mashrur, A. P. Chhoan, S. M. Shahriar, M. F. Haidere, N. J. Runa, S. Kim, D. H. Kweon, H. Hosseinzadeh and J. Y. Cho, *Pharmaceutics*, 2021, **13**, 8894–8918.
2 T. Thi Ngoc Dung, V. Nang Nam, T. Thi Nhan, T. T. B. Ngoc, L. Q. Minh, B. T. T. Nga, V. Phan Le and D. Viet Quang, *Mater. Res. Express*, 2020, **6**, 1250–1259.
3 M. Gautam, D. H. Park, S. J. Park, K. S. Nam, G. Y. Park, J. Hwang, C. S. Yong, J. O. Kim and J. H. Byeon, *ACS Nano*, 2019, **13**, 12798–12809.
4 R. J. Pinto, P. A. Marques, C. P. Neto, T. Trindade, S. Daina and P. Sadocco, *Acta Biomater.*, 2009, **5**, 2279–2289.
5 S. Kittler, C. Greulich, J. Diendorf, M. Koller and M. Epple, *Chem. Mater.*, 2010, **22**, 4548–4554.
6 I. Mohamed Hamouda, *J. Biomed. Res.*, 2012, **26**, 143–151.
7 A. A. Yaqoob, H. Ahmad, T. Parveen, A. Ahmad, M. Oves, I. M. I. Ismail, H. A. Qari, K. Umar and M. N. Mohamad Ibrahim, *Front. Chem.*, 2020, **8**, 341.
8 K. Mijnendonckx, N. Leys, J. Mahillon, S. Silver and R. Van Houdt, *Biometals*, 2013, **26**, 609–621.
9 S. Saengmee-Anupharb, T. Srikhirin, B. Thaweboon, S. Thaweboon, T. Amornsakchai, S. Dechkunakorn and T. Suddhasthira, *Asian Pac. J. Trop. Biomed.*, 2013, **3**, 47–52.
10 D. Guldiren and S. Aydin, *Mater. Sci. Eng., C*, 2017, **78**, 826–832.
11 B. Kwakye-Awuah, C. Williams, M. A. Kenward and I. Radecka, *J. Appl. Microbiol.*, 2008, **104**, 1516–1524.
12 M. Servatan, P. Zarrintaj, G. Mahmodi, S. J. Kim, M. R. Ganjali, M. R. Saeb and M. Mozafari, *Drug Discovery Today*, 2020, **25**, 642–656.
13 Y. Le, P. Hou, J. Wang and J.-F. Chen, *Mater. Chem. Phys.*, 2010, **120**, 351–355.
14 C. C. Chen, H. H. Wu, H. Y. Huang, C. W. Liu and Y. N. Chen, *Int. J. Environ. Res. Public Health*, 2016, **13**, 99.
15 L. Wang, H. He, C. Zhang, L. Sun, S. Liu and R. Yue, *J. Appl. Microbiol.*, 2014, **116**, 1106–1118.
16 X. Wan, L. Zhuang, B. She, Y. Deng, D. Chen and J. Tang, *Mater. Sci. Eng., C*, 2016, **65**, 323–330.
17 K. Sugiura, *US*8313780B2, 2012.
18 A. Panacek, R. Prucek, J. Hrbac, T. Nevecna, J. Steffkova, R. Zboril and L. Kvitek, *Chem. Mater.*, 2014, **26**, 1332–1339.
19 M. Wuithschick, B. Paul, R. Bienert, A. Sarfraz, U. Vainio, M. Sztucki, R. Kraehnert, P. Strasser, K. Rademann, F. Emmerling and J. Polte, *Chem. Mater.*, 2013, **25**, 4679–4689.
20 G. A. Sotiriou, A. Meyer, J. T. Knijnenburg, S. Panke and S. E. Pratsinis, *Langmuir*, 2012, **28**, 15929–15936.
21 T. Cao, W. Tang, J. Zhao, L. Qin and C. Lan, *J. Bionic Eng.*, 2014, **11**, 125–133.
22 X. Jiang, D. Zhang, R. Sun, H. Wang, Y. Yang, H. Guo and Y. Tang, *Appl. Surf. Sci.*, 2021, **542**, 148667.
23 Y. Limami, D. Y. Leger, B. Liagre, N. Pecout and M. Viana, *Eur. J. Pharm. Sci.*, 2021, **158**, 105679.
24 J. Kolmas, E. Groszyk and D. Kwiatkowska-Rozycka, *BioMed Res. Int.*, 2014, **2014**, 178123.
25 M.-l Qi, Z. Huang, A. Phakatkar, W. Yao, Y. Yuan, T. Foroozan, G.-y Xiao, R. Shahbazian-Yassar, Y.-P. Lu and T. Shokuhfar, *CrystEngComm*, 2018, **20**, 1304–1312.
26 C. Guo, Y. Zhang, F. Shao, X. Sheng and Y. Dong, *Micro Nano Lett.*, 2012, **7**, 904–906.
27 C. Guo, J. Xue and Y. Dong, *Mater. Lett.*, 2018, **219**, 182–185.
28 J. Lei, L. Sun, S. Huang, C. Zhu, P. Li, J. He, V. Mackey, D. H. Coy and Q. He, *Am. J. Transl. Res.*, 2019, **11**, 3919–3931.
29 B. A. Jucker, H. Harms and A. J. Zehnder, *J. Bacteriol.*, 1996, **178**, 5472–5479.
30 T. Nomura, Y. Morimoto, H. Tokumoto and Y. Konishi, *Mater. Lett.*, 2008, **62**, 3727–3729.
31 T. Nomura, Y. Morimoto, M. Ishikawa, H. Tokumoto and Y. Konishi, *Adv. Powder Technol.*, 2010, **21**, 8–12.
32 H. Zhou, T. Fan and D. Zhang, *Microporous Mesoporous Mater.*, 2007, **100**, 322–327.
33 H. Zhang, C. Xu, P. Sheng, Y. Chen, L. Yu and Q. Li, *Sens. Actuators, B*, 2013, **181**, 99–103.
34 T. Nomura, S. Tanii, M. Ishikawa, H. Tokumoto and Y. Konishi, *Adv. Powder Technol.*, 2013, **24**, 1013–1016.
35 L. Pla, S. Santiago-Felipe, M. Á. Tormo-Mas, J. Pemán, F. Sancenón, E. Aznar and R. Martínez-Máñez, *Sens. Actuators, B*, 2020, **320**, 128281.
36 Y. H. Lim, K. M. Tiemann, G. S. Heo, P. O. Wagers, Y. H. Rezenom, S. Zhang, F. Zhang, W. J. Youngs, D. A. Hunstad and K. L. J. A. N. Wooley, *ACS Nano*, 2015, **9**, 1995–2008.
37 N. Zhou, L. Wang, P. You, L. Wang, R. Mu and J. Pang, *Int. J. Biol. Macromol.*, 2021, **172**, 515–523.
38 D.-P. Yang, S. Chen, P. Huang, X. Wang, W. Jiang, O. Pandoli and D. Cui, *Green Chem.*, 2010, **11**, 2038–2042.
39 F. Baino and M. Ferraris, *Int. J. Appl. Ceram. Technol.*, 2017, **14**, 507–520.
40 T. He, Y. Weng, P. Yu, C. Liu, H. Lu, Y. Sun, S. Zhang, X. Yang and G. Liu, *J. Phys. Chem. C*, 2014, **118**, 4607–4617.
41 J. Zhang, L. Wang, B. Zhang, H. Zhao, U. Kolb, Y. Zhu, L. Liu, Y. Han, G. Wang, C. Wang, D. S. Su, B. C. Gates and F.-S. Xiao, *Nat. Catal.*, 2018, **1**, 540–546.
42 J. Liu, Y. Yu, Q. Wu and J. Zhang, *Chin. J. Inorg. Chem.*, 2004, **20**, 321–323.
43 C. S. Ciobanu, F. Massuyeau, L. V. Constantin and D. Predoi, *Nanoscale Res. Lett.*, 2011, **6**, 1–8.
44 Y. Yan, X. Zhang, Y. Huang, Q. Ding and X. Pang, *Appl. Surf. Sci.*, 2014, **314**, 348–357.

© 2022 The Author(s). Published by the Royal Society of Chemistry

Open Access Article. Published on 05 August 2022. Downloaded on 5/4/2026 2:56:22 AM.
This article is licensed under a Creative Commons Attribution-NonCommercial 3.0 Unported Licence.

45 O. Akhavan and E. Ghaderi, *Surf. Coat. Technol.*, 2010, **204**, 3676–3683.
46 A. Perdikaki, A. Galeou, G. Pilatos, I. Karatasios, N. K. Kanellopoulos, A. Prombona and G. N. Karanikolos, *ACS Appl. Mater. Interfaces*, 2016, **8**, 27498–27510.
47 Y. Yang, X. Wu, C. He, J. Huang, S. Yin, M. Zhou, L. Ma, W. Zhao, L. Qiu, C. Cheng and C. Zhao, *ACS Appl. Mater. Interfaces*, 2020, **12**, 13698–13708.
48 M. Pica, M. Nocchetti, B. Ridolfi, A. Donnadio, F. Costantino, P. L. Gentili and M. Casciola, *J. Mater. Chem. A*, 2015, **3**, 5525–5534.
49 H. Jia, W. Hou, L. Wei, B. Xu and X. Liu, *Dent. Mater.*, 2008, **24**, 244–249.
50 T. T. T. Vi, S. R. Kumar, J.-H. S. Pang, Y.-K. Liu, D. W. Chen and S. J. Lue, *Nanomaterials*, 2020, **10**, 366–378.
51 A. Pereira, D. T. Reis, K. M. Barbosa, G. N. Scheidt, L. S. da Costa and L. S. S. Santos, *Carbohydr. Res.*, 2020, **488**, 107891.
52 A. Mahanty and D. Shikha, *Int. J. Mater. Res.*, 2021, 922–930, DOI: **10.1515/ijmr-2020-8181**.
53 S. M. Magaña, P. Quintana, D. H. Aguilar, J. A. Toledo, C. Ángeles-Chávez, M. A. Cortés, L. León, Y. Freile-Pelegrín, T. López and R. M. T. Sánchez, *J. Mol. Catal. A: Chem.*, 2008, **281**, 192–199.
54 G. Xu, X. Qiao, X. Qiu and J. Chen, *J. Mater. Sci. Technol.*, 2011, **27**, 685–690.
55 H. Wu, H. Tian, J. Li, L. Liu, Y. Wang, J. Qiu, S. Wang and S. Liu, *Composites, Part B*, 2020, **202**, 108415.
56 S. Unluturk, M. R. Atilgan, A. H. Baysal and M. S. Unluturk, *Int. J. Food Microbiol.*, 2010, **142**, 341–347.
57 V. Lakshmi Prasanna and R. Vijayaraghavan, *Langmuir*, 2015, **31**, 9155–9162.